JOURNAL OF APPLIED PHYSICS **110**, 113909 (2011)

Magnetic properties and short-range structure analysis of granular cobalt silicon nitride multilayers

F. Jiménez-Villacorta,[1,2,a)] A. Espinosa,[2] E. Céspedes,[2] and C. Prieto[2]
[1]*Department of Chemical Engineering, Northeastern University, Boston, Massachusetts 02115, USA*
[2]*Instituto de Ciencia de Materiales de Madrid, Consejo Superior de Investigaciones Científicas. Cantoblanco, 28049 – Madrid, Spain*

(Received 9 August 2011; accepted 1 November 2011; published online 5 December 2011)

The magnetic properties and local order of cobalt/silicon nitride metal-insulator multilayered system have been studied. Magnetization characterization reveals an evolution of the magnetic features by varying the metal layer thickness. Results show that multilayers with larger metal thickness (t) present a pure ferromagnetic character, whereas samples with $t < 2$ nm exhibit a granular superparamagnetic behavior, as it corresponds to discontinuous metal-insulator materials. An important decrease in the magnetization values for the clustered samples has also been observed. X-ray absorption near edge spectroscopy (XANES) and extended x-ray absorption fine structure (EXAFS) at the Co K-edge have been used to determine the local order and electronic configuration around cobalt. Results reveal the formation of an intermediate CoN phase likely located at the Co/Si_3N_4 interface. Further insight in the electronic structure of cobalt atoms has been investigated through *ab-initio* XANES calculations based on Green function's multiple scattering formalism. Local-projected density of states (l-DOS) obtained by simultaneous computations has unveiled the effects of the nitrogen coordination in the electronic structure of the metal atom around the Fermi energy. © *2011 American Institute of Physics*. [doi:10.1063/1.3665877]

I. INTRODUCTION

In the last years, recent advances in the preparation and characterization of magnetic metal-insulator layered and nanostructured systems have boosted their research, not only for potential applications and improvements in the sensor or information technology fields[1,2] but also for their use as model systems for interpretation of the physical phenomena arisen at the nanoscale.[3–5] The accurate tuning of the structural features of such systems provides an indispensable tool to the study of magnetic phenomena arising at the nanoscale. From here, many works have stressed the importance of the metal/ceramic interfaces in the magnetic features of such materials. Structural changes and proximity effects in the contact regions at the interface may lead to modifications of their magnetic properties. For instance, a reduction in the magnetization signal and enhancement of coercivity and anisotropy can be attributed to the formation of an antiferromagnetic oxide or nitride intermediate region at particle/matrix interfaces.[6–8] Also, modifications in the structure at the interface or the chemical bonding between metal atoms and the ceramic matrix at the interface regions can lead to the rise up of ferromagnetic phases at the interface.[9–11]

Furthermore, precise and reliable characterization techniques are essential to understand the basic properties of these materials. In this way, x-ray absorption spectroscopy can play a major role in the study of two-phase nanostructured magnetic materials, due to their sensitivity to any modification in the local symmetry and electronic configuration around a given atom.[12] X-ray absorption near-edge structure (XANES) analysis can be used to correlate the variation of the physical properties of nanoparticle systems and thin films with modifications in the electronic structure through visible evolution in the edge spectral shape.[13,14]

In previous works, transition metal (TM)/silicon nitride multilayers, with TM = Mn, Fe, and Ni, have been studied. Silicon nitride is a promising material to be used as an insulating matrix in metal/ceramic granular systems and multilayers, since it has been found to be a good candidate for applications in electronic devices due to its optical and transport properties, as well as for its chemical inertness at high temperatures.[15–17] We have observed that TM films and particles embedded in a Si_3N_4 matrix display substantial differences in their magnetic properties. For Ni/Si_3N_4, the presence of an interlayer formed by nickel nitride with a rock salt cubic geometry results in a diminution of the magnetic signal of the samples.[18] A reduction of the magnetization is also observed in the Fe systems, with the formation of a non-magnetic zinc-blende FeN phase.[19] However, in Mn/Si_3N_4 multilayers, it has been observed that the formation of a distorted manganese nitride phase induces a ferromagnetic signal in the samples.[20] Recently, metal-silicon nitride systems using Au as an extreme case of heavy atoms have been studied showing no formation of interlayer nitride phase, leading to a well-defined interlayer region.[21]

In this work, we report on the magnetic properties of metal-ceramic multilayered Co/Si_3N_4 systems. Several series of samples, in which the metal layer thickness has been varied, were prepared. Discontinuous metal-insulator multilayers (DMIMs) are ideal candidates for the study of the properties of magnetic granular systems due to their tunability since, for

a)Author to whom correspondence should be addressed. Electronic mail: f.jimenezvillacorta@neu.edu.

instance, the average dimensions of the particles and the interparticle distances can be controlled by the layer thickness, t^n, and thus, to tailor the magnetic interparticle interactions.[22] An extensive study of their magnetic properties has determined the transition from a continuous multilayer to a discontinuous metal-insulator system, below a critical thickness. We have focused our attention on the granular samples, due to their enhanced surface-to-volume ratio. A systematic EXAFS analysis has allowed determination of the local order around cobalt atoms. Finally, XANES analysis within the real-space full multiple scattering formalism has been achieved. XANES computations have been developed to unveil the modifications in the electronic structure of Co, in terms of local-projected density of states (l-DOS), and according to variation in their surrounding symmetry.

II. EXPERIMENTAL

$[Co(t^{Co})/Si_3N_4(3\,nm)]_n$ multilayers were prepared by sequential magnetron sputtering at room temperature on Si(001) substrates. In this paper, we present a study of a series with metal layer thickness from 1 to 5 nm. Two planar 2-inch magnetrons, operated by dc- and RF-power supplies were used. The set-up was controlled by a home-made computer software that allows preparation of multilayers with great precision in the deposition parameters. Si_3N_4 layers were grown with a RF power of 100 W and a deposition rate of about 2 nm/min by reactive sputtering with a working pressure of 6.5×10^{-3} mbar, using a Si target and pure N_2 as a reactive gas to obtain non-oxidized silicon nitride.[23] The base pressure provided by the vacuum system was in the 10^{-7} mbar low range. Co films were deposited with 5.0×10^{-3} mbar pressure of pure Ar by dc-sputtering, being the power supplied less than 10 W and its deposition rate of 1.5 nm/min.

Magnetic measurements were carried out by a SQUID magnetometer (MPMS-5 T from Quantum Design), with the applied field parallel to the film plane. Field cooled magnetization loops were measured at different temperatures, from 5 K to room temperature, after applying a cooling field of 20 kOe. Zero-field cooling–field cooling (ZFC-FC) magnetization curves have been collected at several applied fields, in the intermediate range (from 100 to 1000 Oe).

A detailed study of the short-range structure and the electronic configuration has been developed by x-ray absorption near-edge spectroscopy (XANES) and extended x-ray absorption fine structure (EXAFS) at the Co K-edge. Spectra were measured in the fluorescence yield mode at the Spanish CRG beamline (SpLine, BM25 A) of the European Synchrotron Radiation Facility (ESRF). Details of the experiment were reported elsewhere.[24] EXAFS analysis was performed using the VIPER software.[25] The amplitude and phase functions introduced as inputs in the analysis were obtained by the FEFF8 code.[26] A Fourier transform analysis was performed, using a Hanning window from 3 and 12 $Å^{-1}$in order to filter the EXAFS contributions from the first coordination shells.

Self-consistent XANES calculations at the Co K-edge were achieved using the real-space multiple-scattering formalism of the FEFF8 code.[22] Atomic potentials were approximated by a set of spherical muffin-tin potentials, using the Mattheiss prescription[27] and following the Norman rule for the determination of the atomic radii. Muffin-tin radii were overlapped by a default value of 15% to reduce the effects of discontinuities between adjacent spherical potentials. Self-energy Hedin-Lundqvist corrections were selected for the exchange and correlation potential.[28] An energy dispersion of $\Gamma = 0.8$ eV was introduced in the calculations to account for core-hole lifetime effects and instrumental broadening, and no corrections were made for the Fermi level position. Finally, it should be remarked that XANES and simultaneous electronic structure calculations, in terms of local-projected density of states (l-DOS), were performed within the core-hole final-state and the ground-state approximations.

III. RESULTS AND DISCUSSION

A. X-ray reflectivity

X-ray reflectivity has been measured to estimate the actual thickness of the bilayered structures. Results for the bilayer thickness are shown in Fig. 1. Such an estimation has been obtained using the general expression

$$\theta_m^2 - \theta_c^2 = (m\lambda/2l)^2, \quad (1)$$

where θ_m is the position of the Bragg peaks, θ_c is the critical angle, λ is the x-ray wavelength, and l is the bilayer thickness. Results agree with the estimated nominal thickness. However, no estimation of the thickness for the multilayer with the smallest bilayer thickness could be performed, because it does not present a periodic repetition of the Bragg fringes. The estimated Co layer thickness accounts for an ideal Si_3N_4 thickness of ~3 nm. Simulations of the spectra have been performed with the Xreal software.[29] These simulations mostly reproduce the shape of the experimental data for the two samples with larger bilayer thickness (labeled as $t^{Co} = 4.8$ nm and 3.8 nm), both showing short oscillations

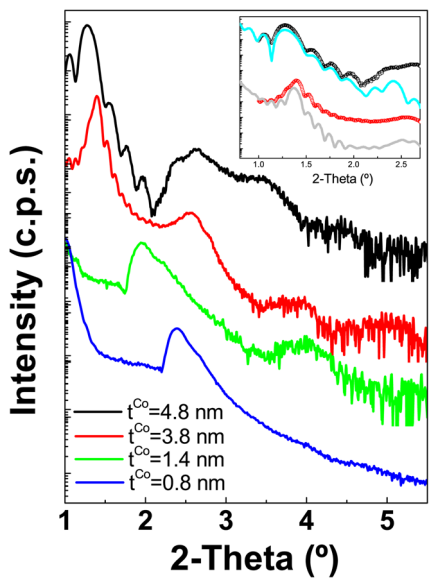

FIG. 1. (Color online) X-ray reflectivity scans for several samples of the Co/Si_3N_4 series. Inset: Fittings obtained for the continuous layered samples.

(Kiessig fringes) related to the total multilayer thickness (inset of Fig. 1). Simulations give similar t^{Co} thickness values as the calculated ones, Si_3N_4 thickness of 3.0 ± 0.3 nm and average roughness about 1.5 nm for both samples. No suitable simulations were found for samples with $t^{Co} \leq 1.4$ nm. This fact, together with the obtained average roughness points out a transition within the samples series, from continuous Co layers for $t^{Co} \geq 3.8$ nm to discontinuous Co embedded in Si_3N_4 for $t^{Co} \leq 1.4$ nm.

B. Magnetization measurements

Figure 2 shows the magnetization loops at different temperatures for samples with nominal thickness $t^{Co} = 3.8$ nm and $t^{Co} = 1.4$ nm. These two samples have been selected here because they clearly illustrate the modification of the magnetic behavior in the continuous-discontinuous transition. The multilayer with $t^{Co} = 3.8$ nm (Fig. 2(a)), presents *M-H* loops with square shapes reaching saturation and reveals a ferromagnetic character retained through the whole temperature range, typical of continuous films. Saturation magnetization value at low temperatures is $0.4\mu_B$/at. Co, reduced gradually as the temperature increases. Also, a slight increase in the magnetization with increasing field in the room temperature loop is observed, suggesting a very small paramagnetic contribution added to the ferromagnetic phase. In contrast, the sample with $t^{Co} = 1.4$ nm (Fig. 2(b)) shows a remarkably different behavior. The obtained M-H loops do not reach saturation, exhibiting clear superparamagnetic (SPM) features, and thus revealing the granular character for such films. Hence, it can be suggested that the specimen consists of a discontinuous metal-insulator system formed by Co clusters embedded in a matrix. A noticeable reduction of magnetization is observed as well to around $0.1\mu_B$/at. Co. Important differences in the coercivity highlight the dissimilar magnetic character of both samples. As it is shown in the inset of Fig. 2(b), coercive field values for the $t^{Co} = 1.4$ nm sample are lower than those exhibited by the multilayer with $t^{Co} = 3.8$ nm, and reaching zero at T = 20 K, as corresponds to a granular sample close to SPM at such low temperature. On the other hand, the $t^{Co} = 3.8$ nm specimen shows a continuous and less sharp diminution of coercivity with increasing temperature, reaching zero oersted at room temperature.

The superposition of the reduced magnetization curves in respect to the reduced field, *H/T*, shown in Fig. 3(a) for $t^{Co} = 2$ nm sample, suggests the existence of a superparamagnetic behavior typical of a non-interacting or weakly interacting particle system. At $T = 10$ K, it can be stated that the majority of particle spins are unblocked and can re-orientate in the direction of the field, with only the largest particles remain blocked and contributing to the small coercivity observed at this temperature. An estimation of the magnetic particle size forming the granular sample can be determined by fitting the SPM loops to the Langevin expression of the magnetization as a function of the applied field and the temperature:

$$M \propto JB_J\left(\frac{\gamma JH}{k_BT}\right), \tag{2}$$

where k_B is the Boltzmann constant and $B_J(x)$, the Brillouin function, is defined as

$$B_J(x) = \frac{2J+1}{2J}\coth\frac{2J+1}{2J}x - \frac{1}{2J}\coth\frac{1}{2J}x. \tag{3}$$

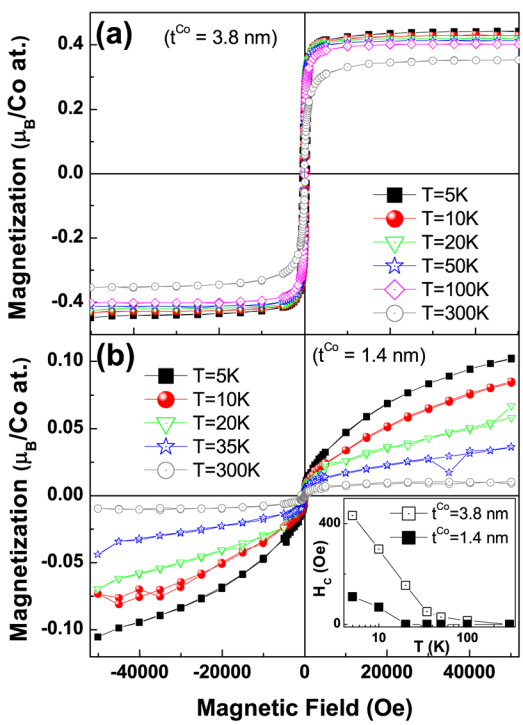

FIG. 2. (Color online) Magnetization loops at different temperatures of [Co (t^{Co})/Si_3N_4 (3 nm)] multilayers: (a) $t^{Co} = 3.8$ nm and (b) $t^{Co} = 1.4$ nm. Inset of (b): Evolution of coercivity with temperature for $t^{Co} = 3.8$ nm and $t^{Co} = 1.4$ nm samples.

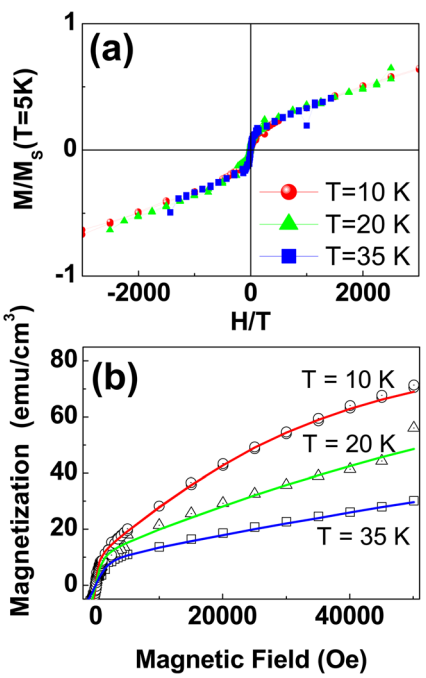

FIG. 3. (Color online) (a) Reduced magnetization of the samples with $t^{Co} = 2$ nm, as a function of H/T. (b) Magnetization curves at T = 10, 20, and 35 K of the granular sample, fitted with the Langevin expression.

A fit has been performed for the loops at three different temperatures: $T = 10$ K, where most of the particles, with dimensions around the average size, are unblocked; and $T = 20$ K and $T = 35$ K, where all the particles are supposed to present an unblocked state. The independent variable J is the total magnetic moment of a spherical cluster that can be useful as an estimation of the cluster size. First attempts to fit the curves have considered one average particle size, and clusters with $D = 5$ Å diameter have resulted to provide the best approximation to the experimental data. However, since a unique size is not able to properly fit the experimental curves, the magnetization curves have been fitted by a sum of Langevin functions. The fittings are depicted in Fig. 3(b). Two representative particle sizes can successfully fit the three $M(H)$ curves, using a majority of particles with a diameter of approximately 5 Å (about 90%) and a non-negligible contribution (around 10%) of larger particles of around 20 Å diameter. These results confirm that cobalt is mainly present in very small aggregates and only a few of them have a size similar to the nominal Co layer thickness.

Figure 4 displays the zero field cooling–field cooling (ZFC-FC) magnetization curves at different applied fields. The curves for $t^{Co} = 3.8$ nm (Fig. 4(a)) present a strong ferromagnetic character up to room temperature. However, some features, as the strong dependence of ZFC magnetization on temperature, resembling the blocking distribution of a magnetic granular system, suggest that, in addition to the ferromagnetic phase, there might be a small contribution of ultrasmall Co particles, manifested as well by the previously mentioned slight increase of magnetization in the saturation range of the loops. Also, in the FC curve at relatively large fields ($H = 1$ kOe), magnetization roughly follows the classical Bloch evolution with temperature for ferromagnetic materials, $M \sim M(0)[1 - BT^{3/2}]$, being $M(0) = 320$ emu/cm^3.

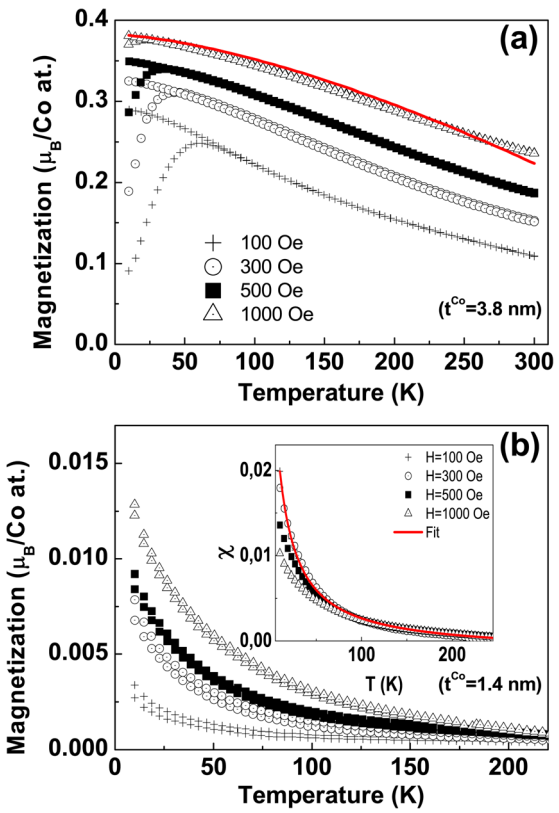

FIG. 4. (Color online) Zero field cooling–field cooling (ZFC-FC) magnetization curves at intermediate fields (from 100 to 1000 Oe) of two different Co layer thickness: (a) $t^{Co} = 3.8$ nm, together with the closest fitting using the Bloch equation, and (b) $t^{Co} = 1.4$ nm, fitted with the Bloch and Curie-Weiss laws. Inset of Fig. (b): Susceptibility of the granular samples, $t^{Co} = 1.4$ nm and corresponding fitting.

Conversely, by lowering the metal layer thickness, substantial differences can be observed (see Fig. 4(b)). Paramagnetic signatures appear in samples with $t^{Co} = 1.4$ nm. ZFC-FC curves exhibit a clear paramagnetic behavior following the Curie-Weiss decay, $M_{FC} \sim C/(T - T^*)$. A typical Curie-Weiss decay is able to reproduce the magnetothermal curves at high enough temperatures down to several K. Differences at very low temperatures may be attributed to the proximity of the particle blocking regime for such granular system. In fact, it seems that the average blocking temperature is below the low limit of measurement (below 10 K), so the peak at the ZFC curve indicating the energy barrier distribution is not observed. A similar evolution of magnetization with temperature has been observed, for instance, in Ni nanoparticles with diameter $D = 5$ nm,[30] diluted Fe particles with average size of $D = 3$ nm in a metallic matrix,[31] or in Co particles with $D = 1.3$ nm dispersed in a ceramic matrix.[1,32] Knowing that the Curie constant is magnetization dependent

$$C = \left(\frac{N_v \mu^2}{3k_B}\right) = \frac{x' V M_S^2}{3k_B}, \tag{4}$$

a convenient fitting would provide additional information of our granular system. Here, N_v is the number of magnetic moments per unit volume, μ is the magnetic moment and k_B is the Boltzmann constant, M_S is the saturation magnetization (in this case cobalt has $M_S = 1440$ emu/cm^3 at 0 K), x' is the volume concentration of the magnetic nanoparticles, and V is the average particle volume ($V = (\pi/6)D^3$, being $D = 6.5$ Å the average particle diameter).[33,34] Thus, an estimation of the volume concentration of the ferromagnetic phase, that is, the particle concentration. By fitting the susceptibility decay, as shown in the inset of Fig. 4(b), an estimation of the magnetostatic interaction degree of particles can be achieved by means of an ordering temperature, T^*.[35] In this case, the ordering temperature is $T^* \approx -6$ K. The negative value of T^* indicates a predominant antiferromagnetic nature of the particle interactions. However, such small value suggests that the granular system is formed by nearly non-interacting magnetic particles. Results also give a particle concentration of $x' \approx 5\%$, much smaller than the expected volume occupation ($\approx 30\%$, based on the estimated thicknesses of the ceramic and metal layers). Nevertheless, this concentration is in agreement with the low magnetization values observed, and with the low degree of interaction between magnetic clusters (for instance, Binns *et al.* estimated concentrations of around $\approx 2\%$ in pure superparamagnetic systems, in detailed studies of granular magnetic systems).[31]

Summarizing so far, we have observed a transition from a ferromagnetic state corresponding to continuous metal-insulator multilayers to noticeable magnetic granular behavior in samples with a metallic layer thickness of about 2 nm.

This layer thickness value is slightly above the percolation threshold observed in many other previous metal-insulator systems, usually around ~1 nm.[4,20,36,37] Thus, an accurate study of the local structure in these metal-insulator multilayers is required for further understanding of their particular structural and magnetic properties.

C. XAS

Representative Fourier transforms (FT) of the EXAFS signals of four Co/Si_3N_4 samples are shown in Figs. 5(a). A reduction of the FT peak around 2.1 Å, attributed to the Co-Co coordination in the metallic phase, is clearly observed as the metal layer thickness decreases. Moreover, a secondary peak, around 1.5 Å, appears. The relative intensity of this peak, in respect to the Co-Co one, increases as the Co layer thickness decreases. Accounting for the distance estimated, and considering that Si coordination with Co typically has a distance around 2.3 Å,[38,39] we can assume that this peak is related to Co-N bonds, likely located at the interface regions. EXAFS analysis has been performed by fitting the contribution to the EXAFS signal provided by the nearest neighbors (see Fig. 5(b)), filtered with a Hanning window in the FT between 0.8 and 2.8 Å. Results of the structural parameters obtained from the EXAFS analysis are displayed in Table I. A clear decrease of the number of Co neighbors as the cobalt layer thickness diminishes is observed. Also, a bump at the right side of the Co-Co peak, at slightly larger distances, becomes more visible. By introducing an added Co-Co coordination shell at around 2.9 Å, coming from tetrahedral CoN phase, the fitting is improved qualitatively. A slight increase of the average coordination number of both neighbors coming from the zinc-blende CoN phase with the reduction of the Co layer thickness is observed. The two samples with thinnest Co layer present similar number of neighbors. Thus, we have found out that Co-N bond at around 1.9 Å and Co-Co coordination at around 2.9 Å, both from an assumed tetrahedral CoN phase, together with the Co-Co coordination at around 2.5 Å typical from the metallic Co *hcp* lattice, are able to reproduce the absorption spectral oscillations. The existence of a visible Co-Co coordination at 2.5 Å confirms the idea that the paramagnetic behavior of the magnetothermal curves are attributable to ultrasmall cobalt grains with very small blocking temperatures for the particles.

TABLE I. Structural parameters obtained from the EXAFS analysis of [Co (t^{Co})/Si_3N_4 (3 nm)] multilayers ($S_0^2 = 0.78$).

Sample	Neighbor	R_j (Å)	N_j	σ^2 (Å^{-2})
Co foil	Co−Co	2.49	12	0.007
[Co (4.8 nm)/Si_3N_4 (3 nm)]	Co−Co	2.51	7.1	0.007
	Co−N	1.93	3.4	0.005
[Co (3.8 nm)/Si_3N_4 (3 nm)]	Co−Co	2.48	4.5	0.010
	Co−N	1.91	3.5	0.008
	Co−Co	2.90	0.8	0.010
[Co (1.4 nm)/Si_3N_4 (3 nm)]	Co−Co	2.53	2.3	0.010
	Co−N	1.93	3.6	0.007
	Co−Co	2.84	1.5	0.006
[Co (0.8 nm)/Si_3N_4 (3 nm)]	Co−Co	2.47	2.3	0.006
	Co−N	1.98	3.2	0.011
	Co-Co	2.93	2.1	0.006

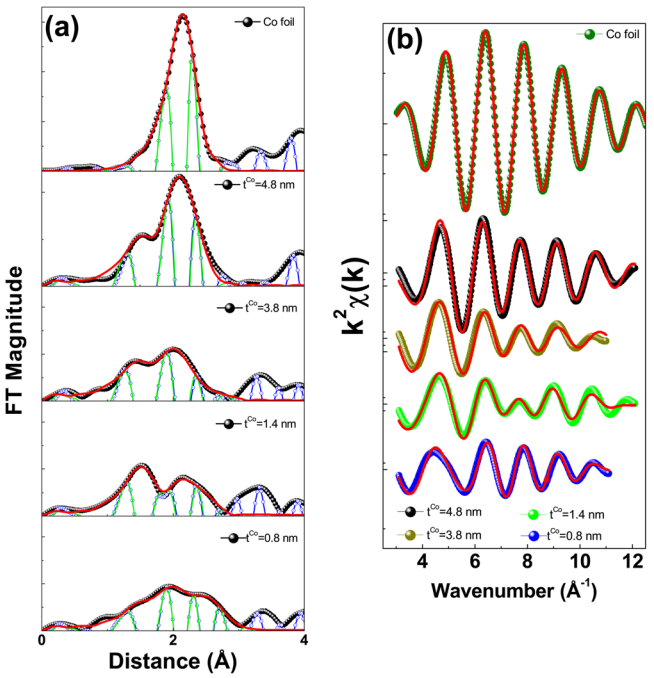

FIG. 5. (Color online) (a) Fourier transforms, and (b) k^3-weighted EXAFS signals filtered to the nearest neighbors at distances below 3.1 Å, for samples of the [Co (t^{Co})/Si_3N_4 (3 nm)] series, and their corresponding fittings. Metal Co foil has been added as a reference.

We can compare all the investigated TM/Si_3N_4 systems, with TM = Fe, Co, Ni and Au, prepared under same experimental conditions. The different TM/Si_3N_4 behavior can be understood regarding the enthalpy of formation (ΔH) of the bulk metal nitrides. ΔH has been pointed out a key parameter in determining the initial chemical bonds at the metal/Si_3N_4 interface, increasing ΔH from Mn to Ni nitrides.[21] No heat of formation has been reported for any gold nitride. For Au/Si_3N_4, where spherical-like Au nanoparticles have been obtained in the Si_3N_4 matrix, a non-reactive Au-Si_3N_4 interface has been shown.[21,40] ΔH has been theoretically calculated for a number of M-nitrides, M_2N, MN, and MN_2, obtaining an increase of the molar enthalpy from Mn to Ni.[41] Considering $\Delta H_{(MN)}$ for instance, $\Delta H_{(MnN)} = -64$ KJ/mol, $\Delta H_{(FeN)} = -16$ KJ/mol, $\Delta H_{(CoN)} = -9$ KJ/mol, and $\Delta H_{(NiN)} = +8$ KJ/mol. The related variation of the nitride phase formed at the M/Si_3N_4 interface, increasing from Mn/Si_3N_4 to Ni/Si_3N_4, can be noticed by the metal/nitride coordination number ratio, CN^{M-M}/CN^{M-N}, obtained by EXAFS. Results from Mn/Si_3N_4 system,[20] Fe/Si_3N_4,[24] Co/Si_3N_4 (this work), and Ni/Si_3N_4 ($t^{Ni} = 3$ nm),[18] depicted in Fig. 6, show a diminution of the relative nitride amount from Mn to Ni in respect to the molar enthalpy. In fact, for Mn/Si_3N_4 ($t^{Mn} = 3.8$ nm), mostly manganese nitride phase was detected by EXAFS,[20] evidencing the M/Si_3N_4 differences. The extreme case is Au/Si_3N_4, because of infinite ratio, due to absence of nitride phase deduced.[21] The stabilization of nitrides instead of silicides, with more negative ΔH in certain cases, has been related to N dangling bonds of Si_3N_4.[21]

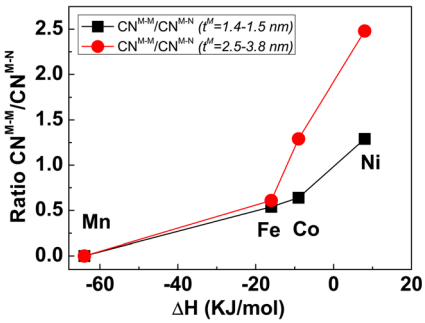

FIG. 6. (Color online) Ratio between the nearest neighbor coordination number for the metal phase, CN^{M-M}, and the coordination number of the nitride phase, CN^{M-N}, for Co and other previously reported transition metals, with $t^M = 1.4-1.5$ nm and $t^M = 2.5-3.8$ nm vs previously reported molar enthalpy.

XANES spectra collected at the Co K-edge are shown in Fig. 7(a). A significant evolution of the edge absorption shape while reducing the metal layer thickness, compared to the cobalt foil reference, is observed. This progressive modification of the XANES spectra can be attributed to a gradual diminution of the metallic phase, followed by an increment of a second contribution with a different geometry around Co atoms. Here, a pre-edge structure at around 7710 eV rises up while decreasing the metal layer thickness. It is known that pre-edge structure in metal K-edge comes from *pd* hybridization effects (*pd* band overlap), characteristic of metal atoms, which present a non-centrosymmetric local geometry, such as the case of tetrahedral environments, well-distorted octahedra, etc. For this reason, considering the metal-ligand distance obtained from the EXAFS analysis, and also due to its bond stability at ambient conditions,[42] we propose an additional contribution formed by zinc-blende cobalt nitride, with a tetrahedral geometry of N atoms around Co absorber. We have carried out XANES calculations for metal Co and for tetrahedral CoN phases. The dimensions of our clusters for calculation were fixed in 6 Å. Self-consistency to produce *ab-initio* calculations of the electronic structure could be achieved with a cluster size of 3 Å. As can be seen in Fig. 7, the new spectral features, indicated by arrows, appeared when the Co thickness decreases are predicted by the computed CoN XANES. Moreover, even if there is not much precision in determining the relative content of both phases, the conclusion is that two different contributions, nanocrystalline metallic and tetrahedrally coordinated phases, are sufficient to reproduce all the experimental features of the XANES spectra.

XANES analysis results to be very useful to determine both structural and electronic features of selected elements in materials. The XANES signal is especially sensitive to the geometrical structure around the absorbing atom, and its features are closely related to the electronic structure of the excited state. Hence, there is a direct connection between the XANES spectral shape and the electronic structure in terms of local-projected density of states (l-DOS).[14,43] The l-DOS has a form similar to the x-ray absorption signal, i.e., $\rho = \rho_0(1+\chi)$, and subsequently $\rho \approx \gamma\mu$, where $\gamma = \rho_0/\mu_0$ is a ratio between smoothly varying atomic background contributions.[44] XANES calculations developed in the FEFF8 code are equivalent to the reciprocal-space Korringa-Kohn-Rostocker band-structure theory, but carried out in the real-space Green's function (RSGF) formalism. Thus, the determination of the electronic structure, by means of calculations of the l-DOS, is analogous to other band-structure calculation methods, like linear augmented plane-wave (LAPW) methods or linear muffin-tin orbital (LMTO) calculations, but in the RSGF

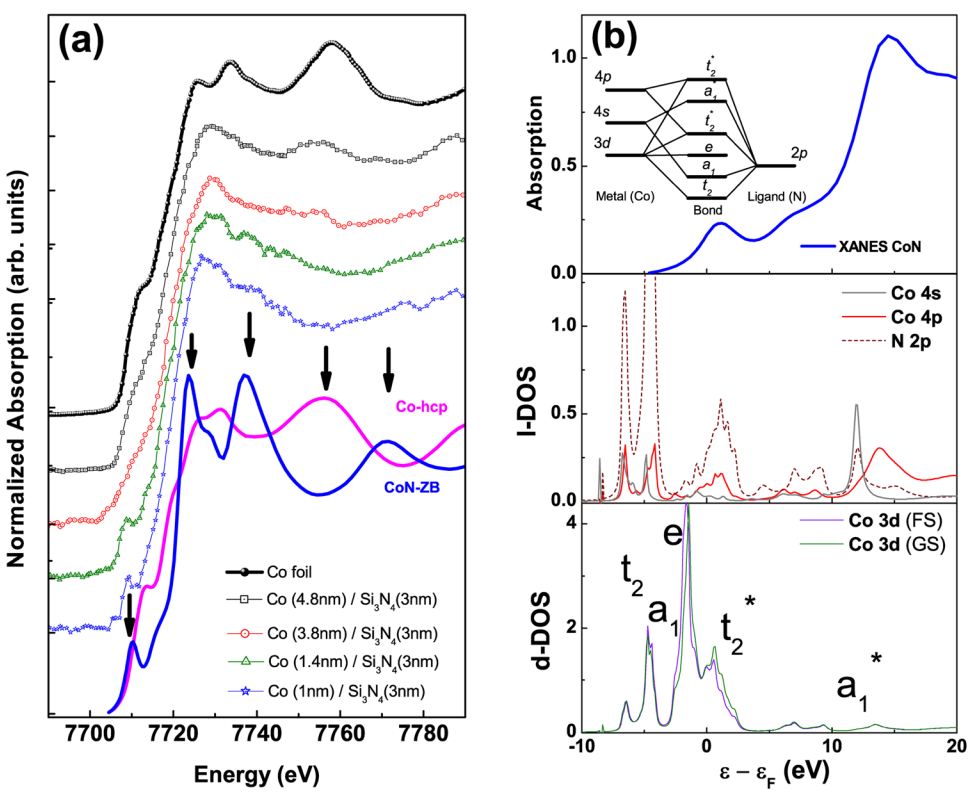

FIG. 7. (Color online) (a) Experimental XANES spectra of [Co (t^{Co})/Si_3N_4 (3 nm)] multilayers and simulations for the contributions of the nanoparticle metallic phase and the CoN intermediate phase; Co foil spectrum has been added as a reference. (b) Calculated XANES spectra and corresponding l-DOS of the CoN phase with tetrahedral geometry, including final state (FS) and ground state (GS) approximations for Co *3d* band.

formalism the treatment accounts for direct experimental results with final-state potentials due to core-hole effects. The information obtained from the quantitative interpretation of spectra based on XANES calculations can be crucial to understand, for instance, the magnetic properties of materials.

Figure 7(b) shows the calculated XANES spectra and their respective projected density of states for the tetrahedral CoN phase. It should be pointed out that computations that reproduce the experimental spectra are performed under the relaxed final-state approximation to simulate the core-hole effects. This may result in a displacement of the *d*-band to lower energies. However, simulations performed in the ground state, without the presence of the core hole, show small differences in respect to the final-state electronic configurations, due to stabilization by chemical bonding of the partially occupied binding states, as can be seen in the figure. In all the cases the calculated XANES spectra follows quite well the broadened shape of the *4p* band above the Fermi energy, ε_F, as it corresponds to a $1s \rightarrow 4p$ transition. *Ab-initio* electronic calculations show the predicted overlap between mixed Co *3d*, Co *4p* and N *2p* states.

As it has been mentioned before, real-space Green's function formalism is a method to determine the electronic structure of a system that in some cases can be analog to other band-structure methods.[45] If we compare the local-DOS obtained by XANES computations with the electronic levels derived from the molecular orbital (MO) theory for tetrahedral metal-ligand coordination (illustrated in the figure), some similarities in the energies close to the Fermi level can be addressed. For instance, from the XANES computations, it is observed that the resonances at around 7 and 4 eV below the Fermi energy, formed by hybridization of the metal *3d* DOS and the *2p* level of the N ligands may correspond to the bonding t_2 state. Bonding a_1 state, below the Fermi level, is mixed with the bonding t_2 state, and would correspond to the regions where Co *4s* band is hybridized with the N *2p* level. At 8 eV above the Fermi level, the hybridized resonant states formed by the metal *4s* and *4p* bands and the ligand *2p* level can be identified as the antibonding a_1^* level in the MO theory. And finally, the two sub-bands around the Fermi energy can be attributed, respectively, to the *e* (at $\Delta E \approx -1.7$ eV, just below the Fermi level) and t_2^* (at the Fermi energy) sublevels, caused by crystal field effects.[46,47] Here, the *e* and t_2 states for tetrahedral symmetry are reversed in respect to the octahedral one, and their label does not include the *g* subscript referring to "gerade" (even) states. Although based on what we have been able to label, these states in MO theory, since t_2 levels are easily distinguished because of the presence of N *2p* contributions, it is worth to notice that still the separation of t_2 and *e* states is not clearly defined (since, for instance, t_2 spreads over the bonding and antibonding regions). The hybridized *p-d* character of the partially unoccupied t_2 level (consisting on mixed metal *3d*, N *2p* and metal *4p* states) is responsible of the pre-edge peak obtained in the experimental and calculated XANES spectra.

In addition, band structure calculations provide another important result. From the band model representation, it is observed that the density of *d*-states of the tetrahedral CoN symmetry at the Fermi level is $N(\varepsilon_F) \approx 1.2$. Hence, we associate the increase in the *d*-bandwidth to ligand-metal overlapping between *p* and *d* states of cobalt and nitrogen, which lowers the d-density of states around the Fermi level. According to the itinerant ferromagnetism model, the Stoner criterion for ferromagnetism relates the ferromagnetic character of a material to the density of states around the Fermi level, thus $N(\varepsilon_F)\, I \geq 1$ (where I is the exchange integral).[48] Using a Stoner exchange parameter for Co of $I = 0.49$ eV,[49] we can observe that the Stoner criterion is not fulfilled. An analog suppression of the ferromagnetism condition by band broadening has been observed in previous works.[50,51] In our case, a reduction of the density of states at the Fermi level as a result of bandwidth broadening leads to a weakening in the condition for ferromagnetism at the CoN interface regions. This interpretation is in full agreement with the decrease in the magnetization values in respect to the Fe bulk one in such multilayered magnetic systems. From here, we can conclude that, differing from analog multilayered systems with Ni, and Mn, and similarly to Fe, nitrogen coordination of *3d* atoms in the case of Co yields the formation of tetrahedral Co-N geometry and leads to a disappearance of the FM signal.

IV. CONCLUSIONS

Magnetic properties and local order of Co/Si_3N_4 multilayers prepared by sequential magnetron sputtering have been studied and correlated to the variation of the metallic layer thickness. A transition from ferromagnetic to superparamagnetic behavior, while decreasing the cobalt layer thickness reveals the formation of discontinuous layers with a granular metal-ceramic structure. Also, a remarkable decrease in magnetization is observed. The magnetic phase of this granular system seems to consist predominantly of ultrasmall particles of around 5 Å, with very weak magnetic interparticle interactions among them.

X-ray absorption spectroscopy has been utilized to assess the local order around cobalt atoms. EXAFS and XANES analyses confirm the existence of Co-N coordination and the formation of a zinc-blende CoN phase, with tetrahedral symmetry around Co atoms, likely distributed at the interface regions between the metal and the insulator. From here, XANES calculations developed to get a further insight in the electronic structure reveal that nitrogen coordination in the tetrahedral geometry results in a broadening of the bands and a subsequent decrease of the density states at the Fermi level. This reduction may explain the weakening of the ferromagnetism condition in such an intermediate phase. From here, we can conclude that the remarkable decrease of magnetization values for the samples, as well as the granular superparamagnetic behavior for the sample with $t^{Co} = 1.4$ nm can be attributed to the formation of a non-magnetic CoN phase, likely located at the interface regions, and also at the boundaries of the Co clusters, providing a physical separation of the metallic Co clusters in the granular sample.

ACKNOWLEDGMENTS

This work was supported by Spanish MICINN Contract No. MAT2009-08786. We acknowledge the European

Synchrotron Radiation Facility for beamtime allocation, and we would like to thank the SpLine CRG beamline staff for assistance during x-ray absorption experiments.

[1]R. Malik, S. Lamba R. K. Kotnala, and S. Annapoorni, Eur. Phys. J. B **74**, 75 (2010).
[2]A. Espinosa, M. García-Hernández, N. Menéndez, C. Prieto, and A. de Andrés, Phys. Rev. B **81**, 064419 (2010).
[3]J. Varalda, G. A. P. Ribeiro, M. Eddrief, M. Marangolo, J. M. George, V. H. Etgens, D. H. Mosca, and A. J. A. de Oliveira, J. Phys. D: Appl. Phys. **40**, 2421 (2007).
[4]J. L. Soroka, V. Stanciu, J. Lu, P. Nordblad, and B. Hjörvarsson, J. Phys.: Condens. Matter **17**, 5027 (2005).
[5]B. J. Hattink, M. García del Muro, Z. Konstantinovic, X. Batlle, A. Labarta, and M. Varela, Phys. Rev. B **73**, 045418 (2006).
[6]A. García-García, A. Vovk, J. A. Pardo, P. Strichovanec, C. Magçen, E. Snoeck, P. A. Algarabel, J. M. de Teresa, L. Morellón, and M. R. Ibarra, J. Appl. Phys. **105**, 063909 (2009).
[7]J. L. Menéndez, G. Armelles, A. Cebollada, F. Briones, F. Peiró, F. Güell, A. Cornet, M. L. Fernández Gubieda, J. Gutiérrez, and C. Meyer, J. Appl. Phys. **89**, 6314 (2001).
[8]J. Arbiol, F. Peiró, A. Cornet, C. Clavero, A. Cebollada, G. Armelles, and Y. Huttel, Appl. Phys. Lett. **86**, 032510 (2005).
[9]M. A. García, F. Jiménez-Villacorta, A. Quesada, J. de la Venta, N. Carmona, I. Lorite, J. Llopis, and J. F. Fernández, J. Appl. Phys. **107**, 043906 (2010).
[10]A. Serrano, E. F. Pinel, A. Quesada, I. Lorite, M. Plaza, L. Pérez, F. Jiménez-Villacorta, J. de la Venta, M. S. Martín-González, J. L. Costa-Krämer, J. F. Fernandez, J. Llopis, and M. A. García, Phys. Rev. B **79**, 144405 (2009).
[11]E. Céspedes, Y. Huttel, L. Martínez, A. de Andrés, J. Chaboy, M. Vila, N. D. Telling, G. van der Laan, and C. Prieto, Appl. Phys. Lett. **93**, 252506 (2008).
[12]M. Benfatto, A. Congiu-Castellano, A. Daniele, and S. Della Longa, J. Synchrotron Rad. **8**, 267 (2001).
[13]S. Nakashima, K. Fujita, K. Tanaka, K. Hirao, T. Yamamoto, and I. Tanaka, Phys. Rev. B **75**, 174443 (2007).
[14]A. L. Ankudinov, J. J. Rehr, J. J. Low, and S. R. Bare, J. Chem. Phys. **116**, 1911 (2002).
[15]M. Vila, E. Román, and C. Prieto, J. Appl. Phys. **97**, 113710 (2005).
[16]K. Remashan, J. H. Jang, D. K. Hwang, and S. J. Park, Appl. Phys. Lett. **91**, 182101 (2007).
[17]M. Gauvin, E. E. Fullerton and F. E. Talke, J. Appl. Phys. **108**, 063925 (2010).
[18]M. Vila, C. Prieto, A. Traverse, and R. Ramirez, J. Appl. Phys. **98**, 113507 (2005).
[19]F. Jiménez-Villacorta, J. Sánchez-Marcos, E. Céspedes, M. García-Hernández, and C. Prieto, Phys. Rev. B **82**, 134413 (2010).
[20]E. Céspedes, E. Román, Y. Huttel, J. Chaboy, J. García-López, A. de Andrés, and C. Prieto, J. Appl. Phys. **106**, 043912 (2009).
[21]E. Céspedes, D. Babonneau, O. Lyon, J. Sánchez-Marcos, S. Rouzière, C. Prieto, L. Olivi, and A. Traverse, J. Appl. Phys. **107**, 104306 (2010).
[22]S. Bedanta, O. Petracic, X. Chen, J. Rhensius, S. Bedanta, E. Kentziger, U. Rücker, T. Brückel, A. Doran, A. Scholl, S. Cardoso, P. P. Freitas, and W. Kleeman, J. Phys. D: Appl. Phys. **43**, 47002 (2010).
[23]M. Vila, D. Cáceres, and C. Prieto, J. Appl. Phys. **94**, 7868 (2003).
[24]F. Jiménez-Villacorta, E. Céspedes, M. Vila, A. Muñoz-Martín, G. R. Castro, and C. Prieto, J. Phys. D: Appl. Phys. **41**, 205009 (2008).
[25]K. V. Klementiev, J. Phys. D: Appl. Phys. **34**, 209 (2001).
[26]A. L. Ankudinov, B. Ravel, J. J. Rehr, and S. D. Conradson, Phys. Rev. B **58**, 7565 (1998).
[27]L. Mattheiss, Phys. Rev. **133**, A1399 (1964).
[28]L. Hedin and B. I. Lundqvist, J. Phys. **C4**, 2064 (1971).
[29]N. D. Telling, S. J. Guilfoyle, D. R. Lovett, C. C. Tang, M.-D. Crapper, and M. Petty, J. Phys. D: Appl. Phys. **31**, 472 (1998).
[30]E. de Biasi, A. León-Vanegas, W. C. Nunes, S. K. Sharma, P. Haddad, T. C. R. Rocha, J. G. Santos Duque, D. Zanchet, and M. Knobel, Eur. Phys. J. **B66**, 503 (2008).
[31]C. Binns, M. J. Maher, Q. A. Pankhurst, D. Kechrakos, and K. N. Trohidou, Phys. Rev. B **66**, 184413 (2002).
[32]J. Nogués, V. Skumryev, J. Sort, S. Stoyanov, and D. Givord, Phys. Rev. Lett. **97**, 157203 (2006).
[33]*Modern Magnetic Materials: Principles and Applications*, edited by R. C. O'Handley (John Wiley and Sons, New York, 2000).
[34]J. Alonso, M. L. Fdez-Gubieda, J. M. Barandiarán, A. Svalov, L. Fernández-Barquín, D. Alba Venero, and I. Orue, Phys. Rev. B **82**, 054406 (2010).
[35]R. W. Chantrell, N. Walmsley, J. Gore, and M. Maylin, Phys. Rev. B **63**, 024410 (2000).
[36]D. Zanghi, A. Traverse, F. Petroff, J. L. Maurice, A. Vaurès, and J. P. Dallas, J. Appl. Phys. **89**, 6329 (2001).
[37]S. Honda, T. Okada, and M. Nawate, J. Magn. Magn. Mater. **165**, 153 (1997).
[38]J. Díaz, R. Morales, S. M. Valvidares, and J. M. Alameda, Phys. Rev. B **72**, 144413 (2005).
[39]C. Jo, D.-C. Kim, and J. I. Lee, J. Magn. Magn. Mater. **306**, 156 (2006).
[40]R. Flammini, F. Wiame, R. Belkou, A. Taleb-Ibrahimi, C. Spezzani, P. Moras, and C. Crotti, J. Appl. Phys. **103**, 083528 (2008).
[41]A. K. Niessen and F. R. De Boer, J. Less-Common Met. **82**, 75 (1981).
[42]P. Lukashev and W. R. L. Lambrecht, Phys. Rev. B **70**, 245205 (2004).
[43]S. K. Pandey, S. Khalid, and A. V. Pimpale, J. Phys. Condens. Matter **19**, 036212 (2007).
[44]J. J. Rehr and A. L. Ankudinov, J. Synchrotron Rad. **8**, 61 (2001).
[45]H. Modrow, S. Bucher, J. J. Rehr. and A. L. Ankudinov, Phys. Rev. B **67**, 035123 (2003).
[46]B. Eck, R. Dronkowski, M. Takashashi, and S. Kikkawa, J. Mater. Chem. **9**, 1527 (1999).
[47]T. E. Westre, P. Kennepohl, J. G. DeWitt, B. Hedman, K. O. Hodgson, and E. I. Solomon, J. Am. Chem. Soc. **119**, 6297 (1997).
[48]*Permanent Magnetism*, edited by R. Skomski and J. M. D. Coey (IOP, Bristol, 1999).
[49]J. F. Janak, Phys. Rev. B **16**, 255 (1977).
[50]K. Kim, U. Yu, Beom, H. Kim, and B. I. Min, J. Phys.: Condens. Matter **18**, 7227 (2006).
[51]V. Iota, J.-H. Park Klepeis, C.-S. Yoo, J. Lang, D. Haskel, and G. Srajer, Appl. Phys. Lett. **90**, 042505 (2007).